Materials Science

AIMS Materials Science, 13(3): 538–559.
DOI: 10.3934/matersci.2026026
Received: 10 February 2026
Revised: 26 May 2026
Accepted: 01 June 2026
Published: 16 June 2026

https://www.aimspress.com/journal/Materials

Research article

Design of melt purification agent for recycled aluminum based on machine learning

Chengbo Li[1], Gangzhi Yu[1], Honglin Zhou[1], Yan Yan[2], Zhaowei Wang[2], Tonghan Yang[1], Chengyi Huang[3], Yuliao Meng[1], Xiaoyang Lu[1], Kaijie Jiang[1], Shuanglan Xie[1] and Cailiu Yin[1,*]

[1] School of Materials and Environment, Guangxi Key Laboratory of Advanced Structural Materials and Carbon Neutralization, Guangxi Minzu University, Nanning 530105, China
[2] Guangzhou Xiaopeng Motors Technology Co，Ltd. Guangzhou 510640, China
[3] ALG Aluminum lnc. Guangxi Key Laboratory of Materials and Processes of Aluminum Alloys, Nanning 530031, China

* **Correspondence:** Email: 20070033@gxmzu.edu.cn.

Abstract: In this study, we proposed a data-driven approach integrating machine learning and experimental validation for the intelligent formula design of melt purification agents for recycled aluminum. Five machine learning algorithms, including random forest regression (RFR), gradient boosting regression (GBR), extreme GBR, polynomial kernel support vector regression, and radial basis function kernel support vector regression, were comprehensively evaluated in terms of root mean square error, mean absolute error, and coefficient of determination. RFR was selected as the optimal model. Combined with Pearson correlation matrix and SHapley Additive exPlanations (SHAP) interpretability analysis, the influence mechanism of each component on the hot-cracking susceptibility and ultimate tensile strength of recycled aluminum alloy was clarified. Multi-objective optimization was carried out to minimize hot-cracking susceptibility and maximize tensile strength, and a novel melt purification agent primarily based on CeF_3 (NF-GX) was developed. The predicted values of hot-cracking susceptibility and tensile strength of NF-GX are 189.97 and 207.80 MPa, respectively, while the corresponding experimental measured values are 214.00 ± 10.39 and 191.33 ± 6.11 MPa, with relative errors of 11.23% and 8.61%. Comparative tests with three commercial purification agents show that NF-GX reduces the metal burn-off rate from 29.19 ± 1.36% to 21.30 ± 0.56%, and refines the average grain size from 191.64 ± 1.98 to 106.36 ± 0.92 μm. Microstructural characterization confirms that the synergistic effect of multi-component fluorides in NF-GX can effectively remove oxide inclusions, break continuous grain boundary liquid films, and induce heterogeneous nucleation, thereby achieving microstructure densification and grain refinement. This study demonstrates that machine learning-driven formula design can break through the limitations of the traditional empirical trial-and-error method, providing a new idea and method for the customized development of high-performance melt purification agents for recycled aluminum.

Keywords: machine learning–driven design; melt purification agent; recycled aluminum alloy; grain refinement; property improvement

1. Introduction

The recycling and reutilization of aluminum resources represent a critical pathway for achieving sustainable development in the aluminum industry. Compared with primary aluminum production, recycled aluminum production can reduce energy consumption by approximately 90% and significantly decrease carbon emissions, delivering substantial economic and environmental benefits [1]. However, owing to the complex and heterogeneous sources of recycled raw materials, elevated impurity levels, and poor stability of the smelting process, recycled aluminum products exhibit considerable performance fluctuations. Consequently, the stabilization of product quality and their deployment in high-performance applications face numerous technical bottlenecks.

During scrap aluminum recycling, surface contaminants on raw materials and the heterogeneous nature of scrap sources inevitably lead to the introduction of non-metallic inclusions and dissolved impurity elements (H, Li, Na, Ca, Mg, and Fe) during the melting stage [2–5]. These impurities tend to form low-melting-point brittle eutectic phases in the final stages of solidification, distributing continuously or in a network-like morphology along grain boundaries. This significantly weakens grain boundary cohesion and induces hot cracking during solidification shrinkage [6–8]. Furthermore, impurity phases and oxide inclusions act as stress concentrators, severely degrading the tensile strength and ductility of the material, thereby hindering the recovery of mechanical properties of recycled aluminum to levels comparable to those of primary aluminum [9,10]. Therefore, high hot-cracking susceptibility and insufficient mechanical performance constitute the two core challenges restricting the efficient and high-value recycling of aluminum resources.

Melt purification agents are critical auxiliary materials in the remelting process of recycled aluminum, effectively suppressing metal burn-off and reducing the generation of inclusions and oxidation products in the melt [9,11]. High-performance purification agents not only purify the aluminum melt and improve fluidity but also refine grain structures by promoting heterogeneous nucleation, thereby suppressing hot cracking at the source and enhancing mechanical properties [12]. Nevertheless, most commercially available melt purification agents are designed for primary aluminum systems, and their formulations fail to adequately address the complex and variable impurity characteristics inherent to recycled aluminum. This results in low purification efficiency in recycled aluminum melts, manifesting as excessive metal loss, aggravated oxidation, insufficient hot-cracking resistance, and limited improvement in mechanical properties. Hence, there is an urgent need to establish novel design methodologies for melt purification agents that are targeted at the impurity profiles of recycled aluminum, enabling customized and precise formulation control.

To address these challenges, we propose an intelligent design methodology for melt purification agents based on machine learning. The extensive application of machine learning (ML) in materials design has provided a novel technological paradigm for optimizing conventional processes. Moreover, researchers have primarily concentrated on the intelligent prediction of melt quality and optimization of process parameters. For instance, Kim et al. [13] employed Gaussian Process Regression (GPR) to achieve high-precision prediction of aluminum melt temperature and hydrogen content, validating the predictive advantages of ML under small-sample conditions. Datta et al. [14] integrated random forest with SHapley Additive exPlanations (SHAP) interpretability methods to quantitatively elucidate the nonlinear correlation between inclusion size and the mechanical properties of aluminum alloys, identifying critical threshold sizes of 5 μm and 10 μm, thereby furnishing quantitative quality-control benchmarks for impurity removal processes.

However, researchers have predominantly focused on unidirectional mapping relationships, such as “process parameters–performance” or “alloy composition–performance,” whereas research directly addressing the formulation design of melt purification agents remains in its infancy. Zhang et al. [15] proposed a flux design strategy for the $NaF–NaCl–Na_2CO_3–CaF_2–Na_3AlF_6$ system based on thermophysical parameters and thermodynamic calculations, screening the optimal formulation through contact angle and purification efficiency tests; however, this approach relies on empirical trial-and-error and extensive experimental validation. Chen et al. [16] constructed a Stacked Neural Network (SNN) by integrating 14 base models, significantly enhancing the prediction accuracy of mechanical properties. Cao et al. [17] applied a machine learning-driven efficient global optimization (EGO) method to the composition design of Al–Zn–Mg–Cu series alloys, successfully developing novel 7xxx series aluminum alloy compositions targeting stress corrosion cracking resistance, corroborating the substantial potential of machine learning in composition optimization of multi-component material systems. Consequently, ML exhibits distinctive advantages in the collaborative optimization of multi-component formulations, nonlinear relationship fitting, and multi-objective optimization, offering significant potential for overcoming the technical limitations of the traditional “empirical trial-and-error” paradigm [18,19].

The machine learning model established in this work was adopted to construct the quantitative relationship between purification agent components and the key performance indicators of recycled aluminum alloy after treatment, including hot-cracking susceptibility and ultimate tensile strength. Based on the research foundation, we systematically trained and compared machine learning algorithms and further developed a novel melt purification agent. Comparative tests were carried out with three commercial purification agents (FY-01, AJ-101A, AJ-01C) to systematically explore the regulation mechanism and action law of the self-developed purifier on the microstructure, hot cracking behavior, and mechanical properties of recycled aluminum alloys. The core novelty of this study lies in applying the machine learning assisted screening framework to the multi-component formula design of recycled aluminum melt purification agents and verifying the effectiveness of the optimized formula through experimental tests.

2. Model construction and purification agent formula design

2.1. Construction and preprocessing of the composition-property dataset

Our core objective of this study was to overcome the limitations of relying on extensive physical trial-and-error in traditional formulation development and to establish a data-driven adaptive design framework. To achieve this and address the practical engineering challenges of high costs and prolonged cycles associated with large-scale aluminum alloy melting and mechanical property prototyping, we moved away from the conventional approach of constructing large-scale datasets relying on pure experiments. Instead, an innovative strategy integrating “core preliminary experiments and physics-informed data augmentation” was adopted to construct an industrially representative dataset comprising 201 independent samples. Among these, 60% were augmented data derived from the parameter ranges of the preliminary fundamental experiments. To prevent the loss of physical significance caused by purely mathematical random generation and to fulfill the requirements of complex machine learning models for exploring the data feature space, the generation of synthetic data strictly adhered to the following two physical and engineering principles [20]: (1) Local Gaussian perturbation based on engineering constraints: considering the inevitable fluctuations during the weighing and mixing of melt purification agent components in industrial production, we utilized the proportional ranges from the preliminary core experiments as anchor points to introduce local Gaussian perturbations to the core slag-forming components (e.g., NaCl and KCl) and key modifiers (e.g.,CeF_3 and CaF_2). This enabled the model to pre-learn the nonlinear impact of “compositional fluctuations” on the final performance, thereby effectively simulating authentic engineering error margins. (2) Performance mapping incorporating metallurgical prior knowledge: when generating comparative samples across a broader span, their performance labels were not randomly assigned; instead, a directional penalty function was constructed based on classical aluminum melt refining mechanisms. With reference to the physical principles of degassing and impurity removal mechanisms by fluoride salts documented in the literature, we incorporated the semi-empirical impact trends of the “fluoride equivalent” within the system on the hot cracking susceptibility and tensile strength. Furthermore, Gaussian white noise was superimposed during the mapping process to simulate testing errors. Consequently, the synthetic data not only covered a broader feature space but also inherently possesssed the correct directional gradients of physical evolution. Within this framework, the model’s input feature space (X) was defined by 12 typical inorganic salt components. The model’s output labels (Y) were designated as the hot cracking susceptibility (HCS) and ultimate tensile strength (UTS), two critical indicators that directly dictate the casting yield and service load-bearing capacity of recycled aluminum. To further ensure data quality and explicitly incorporate material science knowledge, the raw data underwent systematic preprocessing. This included zero-value physical mapping imputation for missing components, outlier detection using the 3σ rule, boxplot methods, and total-sum normalization (mass conservation constraints) to ensure that the components of each sample strictly equaled 100%. These rigorous preprocessing steps compelled the subsequent algorithms to focus on capturing the intrinsic complex mapping relationship between the relative proportional distribution of components and the macroscopic properties.

2.2. Principles and hyperparameter configuration of machine learning regression algorithms

When predicting the mechanical and casting properties of alloys, regression algorithms such as Random Forest, Support Vector Machine, and Artificial Neural Networks are commonly employed in the literature. However, considering that artificial neural networks typically require massive datasets for training, we systematically selected and utilized five representative regression models. This selection was tailored to accommodate the data scale of this research, leverage the advantages of traditional machine learning models in mitigating overfitting on small-to-medium-scale or high-dimensional tabular data, and comprehensively compare the fitting and predictive performances of different underlying algorithms within the multi-dimensional feature space of melt purifiers. Furthermore, to ensure the objectivity of the horizontal comparison among algorithms, mitigate potential overfitting risks, and guarantee the complete reproducibility of the experimental results, rigorous and unified configurations were applied to the core hyperparameters of each model based on statistical learning theory. The specific configuration criteria and theoretical bases were as follows [21–23]: (1) decision tree-based ensemble learning models. Three classical ensemble learning algorithms were selected in this study: Random Forest Regressor (RFR), Gradient Boosting Regressor (GBR), and Extreme Gradient Boosting Regressor (XGBR). For this models, two core parameter constraints were primarily implemented: balanced configuration of base learner scale; and the number of base learners constructed for all three ensemble algorithms was uniformly set to 100. A scale of 100 decision trees was sufficient to ensure that the models significantly reduced prediction variance through majority voting mechanisms or gradient descent strategies. Furthermore, this scale effectively avoided the diminishing marginal utility caused by an overly massive tree network, thereby preventing computational resource waste and the increased risk of overfitting. A strict fixation of the global random state was: given that the underlying mechanisms of ensemble learning algorithms involved random processes, a global random seed was strictly fixed during model construction and dataset splitting to ensure absolute consistency of the input baselines for each algorithmic iteration. (2) Support Vector Machine models (SVM_ Poly, SVM_RBF). For Support Vector Regression, we introduced the polynomial kernel function (poly) and the radial basis function kernel (RBF) to map the 12-dimensional formulation features of the melt purifiers into a higher-dimensional space to identify the optimal regression hyperplane. Unified configuration of the regularization penalty coefficient: in SVM models, the regularization penalty coefficient was the core parameter governing the error tolerance of the model, directly dictating the trade-off between model bias and variance. Moreover, we uniformly calibrated the penalty coefficients for both kernel functions to the classical balanced baseline value. If this value was set too high, the model would severely penalize every training error, leading to excessive distortion of the high-dimensional fitting surface and resulting in overfitting. Conversely, if set too low, the model constraints became overly relaxed, easily causing the omission of critical formulation features and leading to underfitting. Adopting a unified balanced baseline value entailed going from extreme hyperparameter tuning tailored to a single algorithm, aiming to provide a fair platform for algorithmic comparison. This baseline comparison authentically and objectively reflected the intrinsic feature-capturing capabilities and generalization robustness of different kernel functions when dealing with the complex, multivariate data of recycled aluminum melt purifiers.

2.3. Dynamic evaluation strategy for model generalization performance

In traditional materials machine learning research, datasets are conventionally partitioned using a single static ratio (e.g., 8:2), an approach that fails to comprehensively capture the generalization responses of models to varying data scales [24]. To address this limitation, built upon a unified core algorithmic architecture, we introduced a learning curve analysis mechanism to systematically evaluate the fitting capabilities of various algorithms within the feature space. The execution logic was as follows: (1) systematic variation of training set capacity: to investigate the specific impact of the training data volume on the predictive performance of the models, we systematically established seven training set ratio gradients, ranging from 30% to 90% with a fixed step size of 10%. This multi-systematic variation strategy aimed to objectively depict the evolutionary trajectories of the anti-overfitting capabilities and predictive accuracies of algorithms when exposed to different data scales. (2) Hold-out validation under strict variable control: at each specific ratio gradient, the hold-out method was employed to perform a strict partitioning of the 201-sample dataset into training and testing sets. To ensure the rigor of the horizontal comparison, a global random seed was strictly fixed during the data splitting phase. This foundational design guaranteed that, at any given partitioning ratio, the distributions of the training samples employed and the validation sample trajectories remained consistent across all five machine learning models. Although a single hold-out iteration inherently retained some degree of data specificity, by locking the random seed, we effectively isolated the confounding variables introduced by sampling fluctuations, thereby ensuring the objectivity and relative fairness of the multi-algorithm performance evaluation [25,26].

2.4. Evaluation metrics for model predictive performance

Table 1 lists the chemical composition and primary impurity contents of the recycled aluminum alloy used in this study, which belongs to the low-Zn 7xxx series recycled aluminum.

Table 1. Composition and content of recycled aluminum in this study.

Elemental	Mg	Si	Fe	Cu	Mn	Zn	Cr	Other impurities	Al
Value (%)	0.84	0.14	0.093	0.68	0.14	1.53	0.21	<0.3	Balance

To rigorously evaluate model performance and determine the optimal predictive tool, we established a systematic framework for model training and evaluation. Independent predictive models were developed for hot cracking susceptibility and tensile strength, and Model performance was comprehensively evaluated using three metrics: root mean square error (RMSE, Eq 1), coefficient of determination (R^2, Eq 2), and the mean absolute error (MAE, Eq 3).

$$E_{RMSE} = \sqrt{\frac{1}{n}\sum_{i=1}^{n}(y_i - \hat{y}_i)^2} \tag{1}$$

$$R^2 = 1 - \frac{\sum_{i=1}^{n}(y_i-\hat{y}_i)^2}{\sum_{i=1}^{n}(y_i-\bar{y})^2} \tag{2}$$

$$E_{MAE} = \frac{1}{n}\sum_{i=1}^{n}|(y_i - \hat{y}_i)| \tag{3}$$

In the equations, i denotes the index of each sample included in the evaluation, and n is the total number of samples. y_i and $\hat{y}_i$ represent the experimental and predicted values of the i sample, respectively, while $\bar{y}$ is the mean of the experimental values for all samples. MAE and RMSE reflect the overall deviation between the experimental and predicted values across all samples, whereas R^2 measures the correlation between them. A high-accuracy machine learning model is characterized by a larger R^2 and smaller MAE and RMSE values.

Using the above formulas, the performance metrics of five regression models were calculated under different training set ratios. Line graphs were then employed to systematically compare model performance in predicting hot-cracking susceptibility and tensile strength.

For the prediction of hot-cracking susceptibility, as illustrated by the RMSE and MAE line charts in Figure 1, the prediction errors did not exhibit a monotonic decrease as the training set proportion increases. Instead, when the training set ratio ranged from 0.3 to 0.8, the errors of the models fluctuated within a certain range. However, when the training set ratio reached an extreme of 0.9, RMSE and MAE for all models increased significantly, indicating a significant deterioration in predictive performance. This phenomenon was primarily attributed to the excessively small test set at this ratio, which induced high variance and instability in the evaluation results. Notably, RFR and GBR demonstrated the best overall stability and the lowest error levels. In contrast, XG Boost performed sub optimally, with prediction errors noticeably higher than those of RFR, GBR, and SVM_ Poly. Support Vector Regression with a radial basis function kernel (SVM_RBF) consistently exhibited the largest prediction errors across all partitioning ratios.

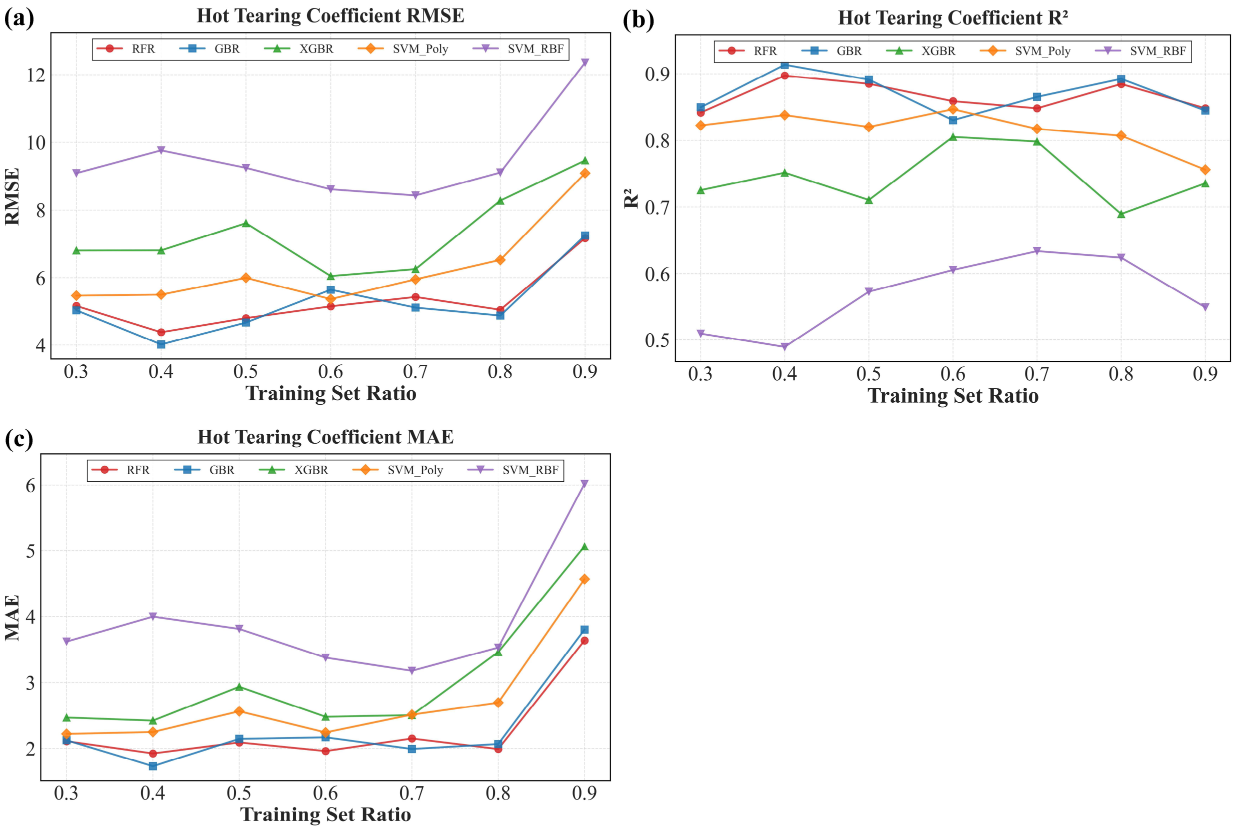

Figure 1. Effect of training set proportion on (a) RMSE; (b) R^2; and (c) MAE for hot tearing coefficient prediction.

For tensile strength prediction, all models achieved better overall predictive accuracy relative to hot-cracking susceptibility, as illustrated in Figure 2 RFR, GBR, and SVM _Poly achieved the best predictive results. For training set ratios between 0.3 and 0.8, these three models maintained low RMSE and MAE values and exhibited consistently high coefficients of determination (R^2 approaching 0.9), indicating their effectiveness in capturing the complex nonlinear relationships between tensile strength and melt purification agent composition. However, similar to the trend observed in hot-cracking susceptibility, when the training set ratio reached the extreme of 0.9, the errors for all models showed a noticeable exhibit a significant increase due to the drastic reduction in test set samples. Furthermore, the overall predictive accuracy of XG Boost was distinctly inferior to the aforementioned three models, with its errors demonstrating a gradual upward trend as the training set ratio increased. Moreover, SVM_RBF displayed significant instability, exhibiting excessively high errors at smaller training sample sizes.

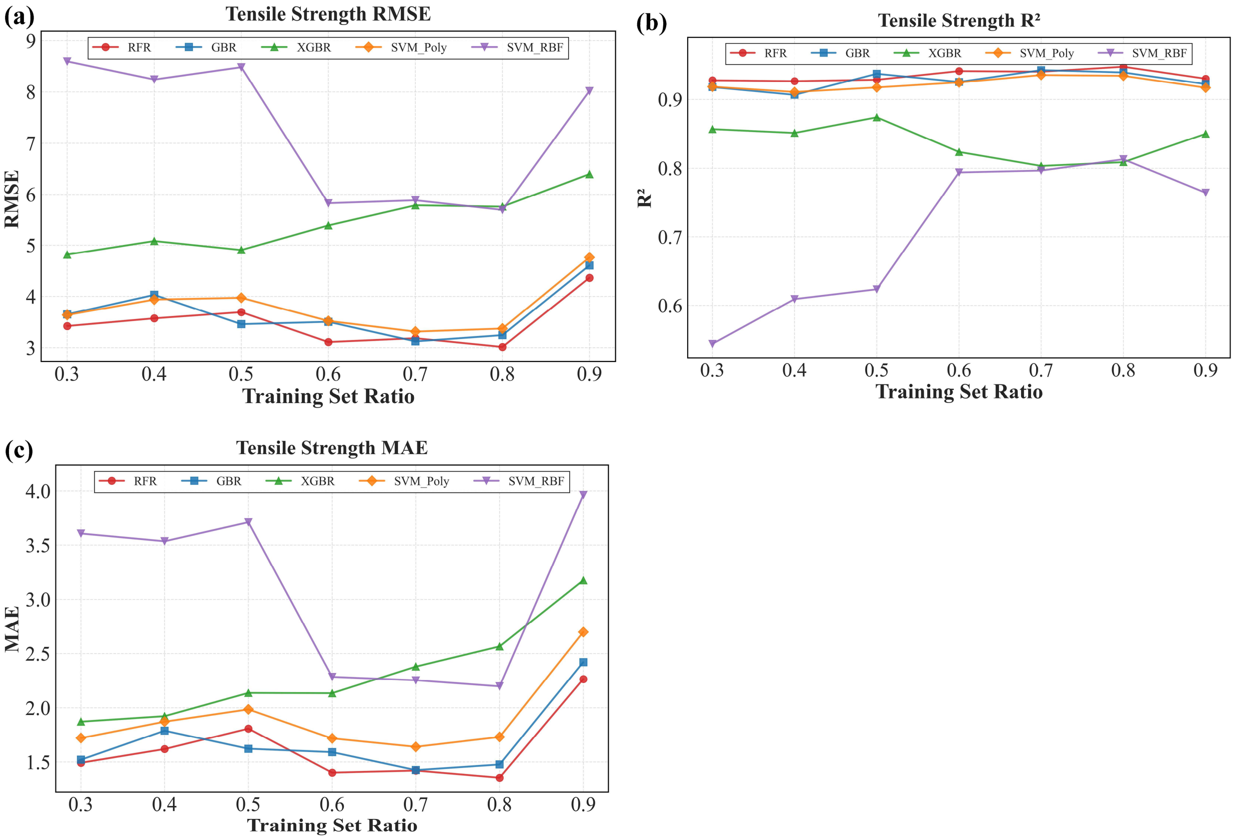

Figure 2. Effect of training set proportion on (a) RMSE; (b) R^2; and (c) MAE for tensile strength prediction.

To comprehensively evaluate the overall performance of the algorithms across dual prediction targets and training set ratio gradients, we introduced a comprehensive scoring metric based on normalization. Considering that the root mean square error (RMSE) carries actual physical units (e.g., MPa) and cannot be directly subjected to algebraic operations with the dimensionless coefficient of determination (R^2), we extracted the average R^2 ($\overline{R^2}$) and the average RMSE ($\overline{RMSE}$) of each model across all training set ratios. The $\overline{RMSE}$ was then mapped to a 0-1 interval via Min-Max normalization ($\overline{RMSE}_{norm}$). To ensure that a lower error positively contributed to the final score, the normalized RMSE was inverted as ($1-\overline{RMSE}_{norm}$). The comprehensive score (Score, out of 100) was calculated as shown in Eq 4:

$$\text{Score}=\left(\text{w1}\times\overline{\text{R}^2}+\text{w2}\times(1-\overline{\text{RMSE}}_{\text{norm}})\right)\times 100 \tag{4}$$

In the main analysis, the weight factors were set as w1 = w2 = 0.5 to give equal importance to goodness of fit and absolute error control capability. Furthermore, to ensure the objectivity of model selection and eliminate potential bias from specific weight assignments, sensitivity analyses were conducted using alternative weighting schemes (e.g., 0.6/0.4 and 0.4/0.6). The consistent ranking results across these schemes confirmed that the selection of the RFR model was robust and independent of the specific weighting configuration.

A higher comprehensive score indicated better overall predictive performance of the algorithm. The calculated results, illustrated in Figure 3, demonstrated that the RFR model achieved the highest score among the five algorithms. This model consistently maintained high accuracy and stability across both prediction tasks. Therefore, we selected RFR as the core predictive model for the subsequent formulation optimization.

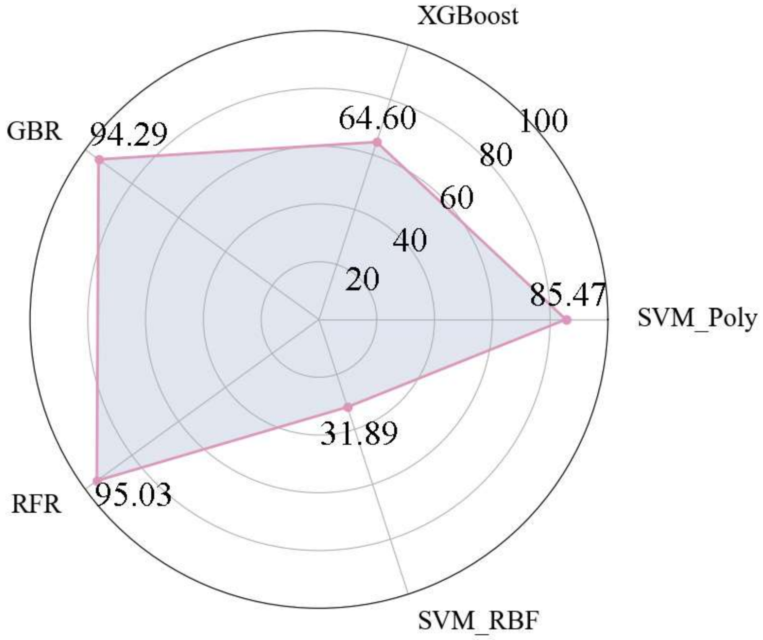

Figure 3. Scores of machine learning models.

2.5. *Mechanism analysis of composition-property mapping based on model interpretability and feature engineering*

To break the "black-box" nature of machine learning and elucidate the intrinsic driving mechanisms of various melt purifier components on the final properties of recycled aluminum alloys, we integrated a feature correlation matrix with the SHAP framework to conduct an in-depth global interpretability analysis of the best-performing RFR model.

Figure 4 displays the Pearson correlation coefficient matrix among the 12 inorganic salt features. Here, NaCl and KCl exhibited a highly positive correlation ($r = 0.83$), which accurately reflected the a priori engineering fact that the industry typically utilized equimolar or fixed-ratio chloride salts as the base flux. Notably, the base salts (NaCl and KCl) showed significant negative correlations (ranging from −0.61 to −0.71) with the core functional additives in the system (e.g., Na_2SiF_6, NaF, Na_2SO_4, $CaCO_3$). This feature distribution indicated a "trade-off under mass conservation constraints" in formulation design: increasing the proportion of active salts to enhance specific metallurgical functions (such as degassing, slagging, or exothermic reactions) inevitably diluted the concentration of the base salts. This provided a critical material constraint background for subsequently interpreting the model's predictive behavior.

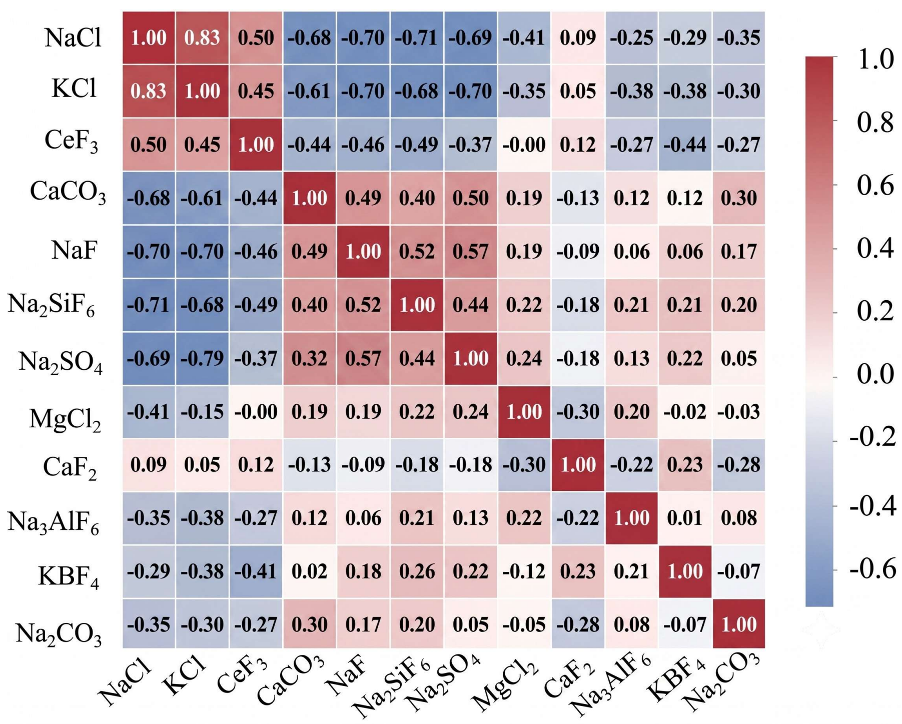

	NaCl	KCl	CeF_3	$CaCO_3$	NaF	Na_2SiF_6	Na_2SO_4	$MgCl_2$	CaF_2	Na_3AlF_6	KBF_4	Na_2CO_3
NaCl	1.00	0.83	0.50	-0.68	-0.70	-0.71	-0.69	-0.41	0.09	-0.25	-0.29	-0.35
KCl	0.83	1.00	0.45	-0.61	-0.70	-0.68	-0.70	-0.35	0.05	-0.38	-0.38	-0.30
CeF_3	0.50	0.45	1.00	-0.44	-0.46	-0.49	-0.37	-0.00	0.12	-0.27	-0.44	-0.27
$CaCO_3$	-0.68	-0.61	-0.44	1.00	0.49	0.40	0.50	0.19	-0.13	0.12	0.12	0.30
NaF	-0.70	-0.70	-0.46	0.49	1.00	0.52	0.57	0.19	-0.09	0.06	0.06	0.17
Na_2SiF_6	-0.71	-0.68	-0.49	0.40	0.52	1.00	0.44	0.22	-0.18	0.21	0.21	0.20
Na_2SO_4	-0.69	-0.79	-0.37	0.32	0.57	0.44	1.00	0.24	-0.18	0.13	0.22	0.05
$MgCl_2$	-0.41	-0.15	-0.00	0.19	0.19	0.22	0.24	1.00	-0.30	0.20	-0.02	-0.03
CaF_2	0.09	0.05	0.12	-0.13	-0.09	-0.18	-0.18	-0.30	1.00	-0.22	0.23	-0.28
Na_3AlF_6	-0.35	-0.38	-0.27	0.12	0.06	0.21	0.13	0.22	-0.22	1.00	0.01	0.08
KBF_4	-0.29	-0.38	-0.41	0.02	0.18	0.26	0.22	-0.12	0.23	0.21	1.00	-0.07
Na_2CO_3	-0.35	-0.30	-0.27	0.30	0.17	0.20	0.05	-0.05	-0.28	0.08	-0.07	1.00

Figure 4. Pearson correlation heatmap of 12 key components in melt purification agents.

Figure 5a reveals the global feature contributions when the RFR model predicted the hot tearing coefficient. In the SHAP summary plot, features were ranked from top to bottom based on their mean absolute impact on the model output, with red dots representing high concentrations of the feature and blue dots representing low concentrations. The results indicated that Na_2SiF_6, $CaCO_3$, and Na_2SO_4 are the dominant factors affecting the hot cracking performance of the alloy. The plot shows that high values (red dots) for these three components are concentrated in the positive SHAP value region (i.e., they drove up the hot tearing coefficient, exerting a deteriorating effect). From a metallurgical physical mechanism perspective, the high-temperature decomposition of $CaCO_3$ generated rapid gas evolution, while excessive Na_2SO_4 could trigger exothermic reactions. These significant physicochemical interactions could easily disrupt the fragile dendritic interlocking skeleton of 7xxx series high-strength aluminum alloys during the terminal stage of solidification, thereby significantly increasing the risk of liquid film tearing. Conversely, high values of NaCl and KCl (red dots) were distributed in the negative SHAP value region, indicating that a sufficient base chloride melt provided a stable refining environment, effectively mitigating hot cracking susceptibility. For the global SHAP explanation for tensile strength shown in Figure 5b, the influence of Na_2SO_4 became the dominant factor and exhibited a significant detrimental effect: highly negative SHAP values (significantly reducing mechanical properties). This suggested that in the melting system of 7xxx series recycled aluminum, sulfates may introduce difficult-to-remove sulfide inclusions or exacerbate the oxidation melting loss of the melt, acting as a “critical defect initiation site” for mechanical properties. Concurrently, NaCl and KCl once again demonstrated a beneficial effect on strength (red dots correspond to positive SHAP values).

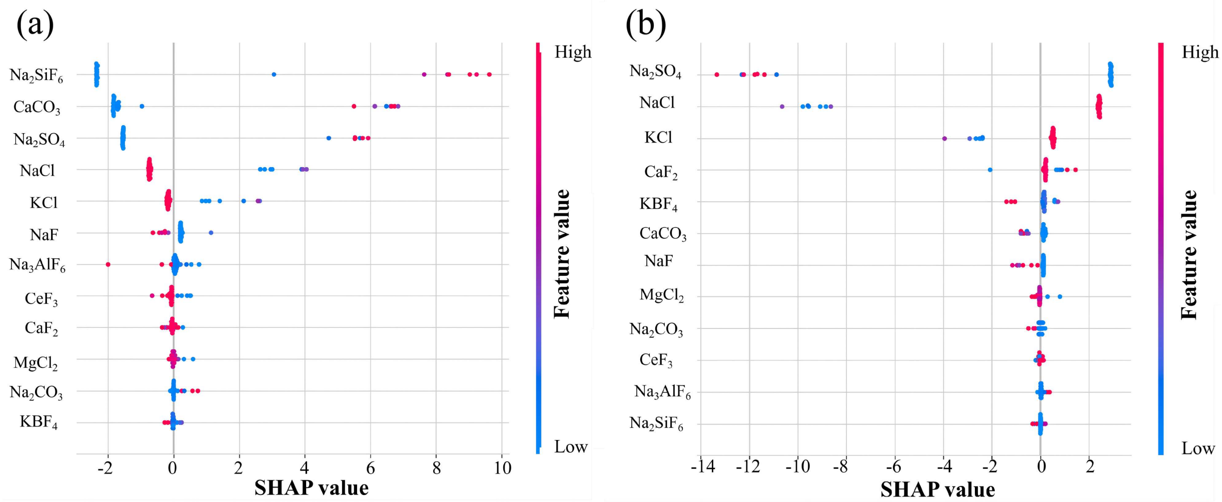

Figure 5. SHAP summary plots of the optimal RFR model for predicting: (a) hot tearing coefficient and (b) tensile strength.

Based on the evaluation results, the RFR model was selected to guide the design of the purification agent and predict its performance indicators. By predicting and screening candidate compositions, a novel melt purification agent primarily based on CeF3 (NF-GX) was successfully developed. The detailed chemical composition of NF-GX is presented in Table 2, and its corresponding predicted performance indicators are summarized in Table 3.

Table 2. Composition and content of NF-GX.

Composition	NaCl	KCl	CeF_3	NaF	Na_2SO_4	$MgCl_2$	CaF_2	Na_3AlF_6	KBF_4	Na_2CO_3
Value (%)	30.02	30.05	11.94	0.01	0.05	5.01	7.99	4.84	4.91	5.18

Table 3. Predicted values for NF-GX performance.

Performance index	HCS	UTS (Mpa)
Predicted value	189.97	207.80

3. Materials and methods

3.1. Materials

In this study, a recycled aluminum alloy with a composition consistent with the model training dataset (see Table 1) was selected as the experimental material to evaluate the purification performance of the novel melt purification agent. The composition of the novel agent was determined based on predictions from the RFR model and was designated NF-GX, with its specific composition listed in Table 2. For comparative evaluation, three commercially available general-purpose melt purification agents (FY-01, AJ-101A, and AJ-01C) were selected as reference samples. The chemical compositions of these agents are presented in Tables 4 to 6.

Table 4. Composition and content of FY-01.

Composition	NaCl	KCl	$CaCO_3$	NaF	Production company
Value (%)	45	35	15	5	Zhenghua Die Casting

Table 5. Composition and content of AJ-101A.

Composition	NaCl	KCl	Na_2SiF_6	Na_2SO_4	Production company
Value (%)	50	40	6	4	Sichuan Land

Table 6. Composition and content of AJ-01C.

Composition	NaCl	KCl	Na_2SiF_6	$MgCl_2$	$CaCO_3$	NaF	Production company
Value (%)	40	35	7	5	5	8	Devi Technology

3.2. Experimental methods

All comparative experiments in this study were performed under uniform and standardized conditions with strict control of raw materials, melting parameters, purification agent dosage, and testing procedures to ensure result repeatability and statistically significant differences between groups. The addition amount of the melt purification agent was uniformly set at 0.3 wt%, which was determined as the optimal dosage based on industrial practice and preliminary experiments. This dosage ensured sufficient purification efficiency while avoiding adverse effects caused by excessive flux. The melt purification agent was tightly wrapped in aluminum foil and pressed into 2 kg of recycled aluminum preheated to the semi-solid state at 610 ± 5 ℃ (solid–liquid two-phase region). The temperature was raised to 720–740 ℃ at a rate of 10 ℃/min using a programmed resistance furnace to fully melt the alloy, after which surface dross was promptly skimmed off. No additional argon degassing was conducted during the experiments. The melt was held at 720 ℃ for 5 min to enable sufficient flotation of inclusions, after which surface dross was skimmed again immediately before casting.

Oxidation loss rate measurement: a fixed mass of recycled aluminum was used for each group. The initial mass of raw material before melting and the total mass of qualified castings after melting and casting were recorded separately. The oxidation loss rate was calculated as follows: oxidation loss rate = (initial total mass − total mass of castings)/initial total mass × 100%. Triplicate parallel experiments were conducted for each group, and the results are expressed as mean ± standard deviation.

The hot-cracking susceptibility of the alloy was evaluated using a constrained bar hot-crack mold. The mold cavity contained four cylindrical constraint bars, each with a diameter of 9.5 mm and lengths of 51, 89, 127, and 165 mm. One end of each bar was constrained by a Φ29 mm sprue, and the other end by a Φ19 mm spherical cavity, with a center-to-center spacing of 38 mm. For each alloy, three hot-crack samples were cast. The length, position, and severity of cracks along the constraint bars were visually inspected, and the hot-cracking susceptibility coefficient (HCS) was calculated as Eq 5:

$$HCS=\sum(F_l \times F_{lc} \times F_c) \qquad (5)$$

where F_l, F_{lc}, and F_c are the weighting factors corresponding to crack length, position, and severity, respectively. Higher HCS values indicated greater susceptibility to hot cracking.

Tensile tests were carried out at room temperature using a WDW-100E microcomputer-controlled electronic universal testing machine with a rated load of 100 kN and a crosshead speed of 1 mm/min. Three parallel specimens were tested for each group, and the results are presented as mean ± standard deviation. Specimens with dimensions of 15 × 15 × 5 mm were cut from the same position of each casting using a wire-cut electrical discharge machine. The specimens were successively ground with abrasive papers from 180# to 2000# and then polished to a scratch-free mirror surface using a P-1 metallographic polishing machine. The polished specimens were etched with Keller's reagent for 15 s, rinsed with distilled water and anhydrous ethanol sequentially, and dried by cold air. Microstructural observations were performed under an IE-300W inverted metallurgical microscope at 200× magnification. The morphology and distribution of inclusions as well as tensile fracture characteristics were analyzed using a ZEISS EVO 18 scanning electron microscope (SEM) operated at an accelerating voltage of 20.00 kV equipped with an energy-dispersive X-ray spectrometer (EDS). The average grain size was quantitatively determined using Image-Pro Plus 6.0 software based on at least 10 fields of view for each specimen to systematically evaluate the effect of melt purification agents on the microstructure of recycled aluminum alloys.

4. Results and discussion

4.1. Effect of different melt purification agents on the oxidation loss of recycled aluminum

The oxidation loss rate reflected the protective ability of melt purification agents on the melt surface. The oxidation loss of recycled aluminum treated with different melt purification agents is shown in Figure 6. The control group (without any melt purification agent) exhibited a loss rate of 29.19 ± 1.36%. The oxidation losses of the experimental groups were reduced to 23.78 ± 0.68% for FY-01, 26.14 ± 0.19% for AJ-101A, 24.66 ± 0.37% for AJ-01C, and 21.30 ± 0.56% for the machine learning–designed NF-GX. The results indicated that the use of melt purification agents can significantly reduce the oxidation loss of recycled aluminum. Among them, NF-GX exhibited the best protective effect, with a loss rate nearly 10% lower than the control group. Its superior performance was mainly attributed to its multi-component composition, containing 11.94% CeF_3, 7.99% CaF_2, 4.84% Na_3AlF_6, and 4.91% KBF_4, which formed a multicomponent protective system. In contrast, other commercial melt purification agents were primarily binary systems composed of NaCl and KCl, providing relatively limited protection. The synergistic action of multiple fluorides in NF-GX enabled the formation of a denser protective layer on the melt surface, effectively isolating the melt from oxygen and thereby significantly reducing the oxidation loss of alloying elements.

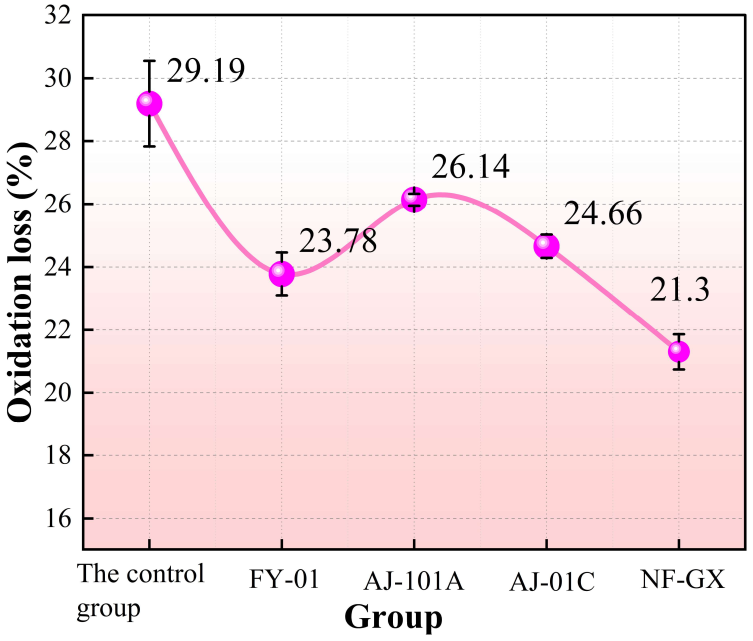

Figure 6. Oxidation loss of recycled aluminum treated with different melt purification agents.

4.2. Effects of different melt purification agents on hot-cracking and mechanical properties

The hot-cracking susceptibility and mechanical properties of the recycled aluminum alloy under different melt purification treatments are presented in Figure 7. The untreated alloy exhibited a high HCS of 325.33 ± 11.55, indicating a strong tendency for hot cracking during the final stage of solidification. After the addition of conventional melt purification agents (FY-01, AJ-101A, and AJ-01C), the HCS values decreased to 318.67 ± 11.55, 301.33 ± 9.24, and 293.33 ± 4.62, corresponding to reductions of 2.04%–9.83%. This result indicated that conventional agents can partially alleviate hot cracking. In contrast, treatment with the novel melt purification agent NF-GX reduced the HCS markedly to 214.00 ± 10.39, representing a 34.22% decrease compared with the untreated alloy and the best resistance to hot cracking. The model predicted an HCS value of 189.97 for this formulation, corresponding to a relative error of 11.23%.

As shown in Figure 7a, the untreated alloy exhibited a tensile strength of 152 ± 3 MPa. All melt purification treatments resulted in higher tensile strength. The tensile strength increased to 169.33 ± 3.51 MPa for FY-01, 172.00 ± 3MPa for AJ-101A, and 178.33 ± 3.06 MPa for AJ-01C, corresponding to improvements of 11.4%–17.32%. The highest tensile strength, 191.33 ± 6.11 MPa, was achieved with NF-GX, representing a 25.87% increase compared with the untreated alloy and indicating a pronounced strengthening effect. The predicted tensile strength for this formulation was 207.80 MPa, corresponding to a relative error of 8.61%.

The simultaneous improvement in hot-cracking resistance and tensile strength can be explained by liquid-film theory and melt purification mechanisms [6,27–30]. In the untreated alloy, continuous low-melting liquid films readily form along grain boundaries. Moreover, oxide inclusions act as stress concentrators and stabilize these liquid films by modifying the eutectic distribution. As a result, hot cracking occurs easily under solidification shrinkage stresses. Conventional purification agents, such as FY-01, mainly remove inclusions through physical adsorption. This process reduces the continuity of grain-boundary liquid films and leads to moderate improvements in hot-cracking behavior and mechanical properties. By contrast, the NF-GX composite agent, based on the synergistic effects of the CeF_3–KBF_4–Na_3AlF_6 system, enables deeper melt purification and significant grain refinement. This treatment breaks continuous liquid films into discontinuous, isolated regions. In addition, the segregation of active elements at grain boundaries alters the physicochemical properties of the liquid films. These effects enhance grain-boundary cohesion and healing at high temperatures, thereby markedly reducing hot-cracking susceptibility while improving tensile strength.

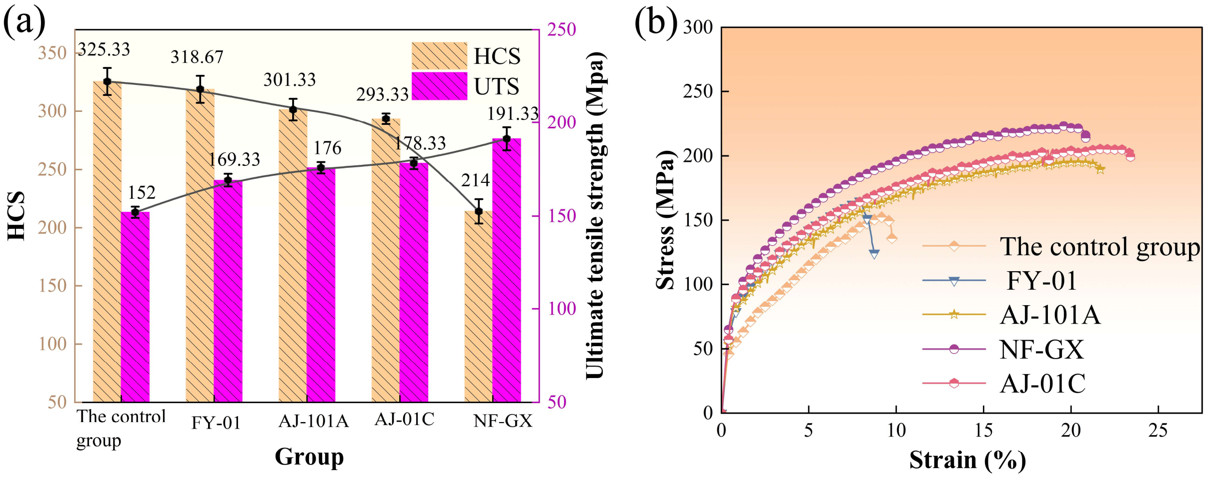

Figure 7. Effects of different melt purification agents on the hot-cracking behavior and mechanical properties of the alloy: (a) hot-cracking susceptibility coefficient and UTS; and (b) stress-strain curve.

4.3. Effect of melt purification agents on the microstructure of recycled aluminum alloy

To investigate the influence of melt purification agents on the as-cast microstructure of recycled aluminum alloy, samples treated with different agents were analyzed by optical microscopy, SEM, EDS, and tensile fracture surface observation. The optical microscopy results in Figure 8 show that the untreated alloy exhibits coarse dendritic grains with an average size of 191.64 ± 1.98 μm. The addition of melt purification agents achieved obvious grain refinement, and the refining effect was enhanced with the increase in compositional complexity of the purifiers. The average grain size was reduced to 138.14 ± 0.98 μm by FY-01, approximately 115.45 ± 0.87 μm by AJ-101A, and 115.16 ± 1.02 μm by AJ-01C. In comparison, the newly developed NF-GX further refined the grains to 106.36 ± 0.92 μm. The superior refinement achieved by NF-GX was attributed to its multi-component system (CeF_3, KBF_4, Na_3AlF_6), which likely formed high-melting-point dispersoids such as CeO_2 and AlB_2, serving as effective heterogeneous nucleation sites.

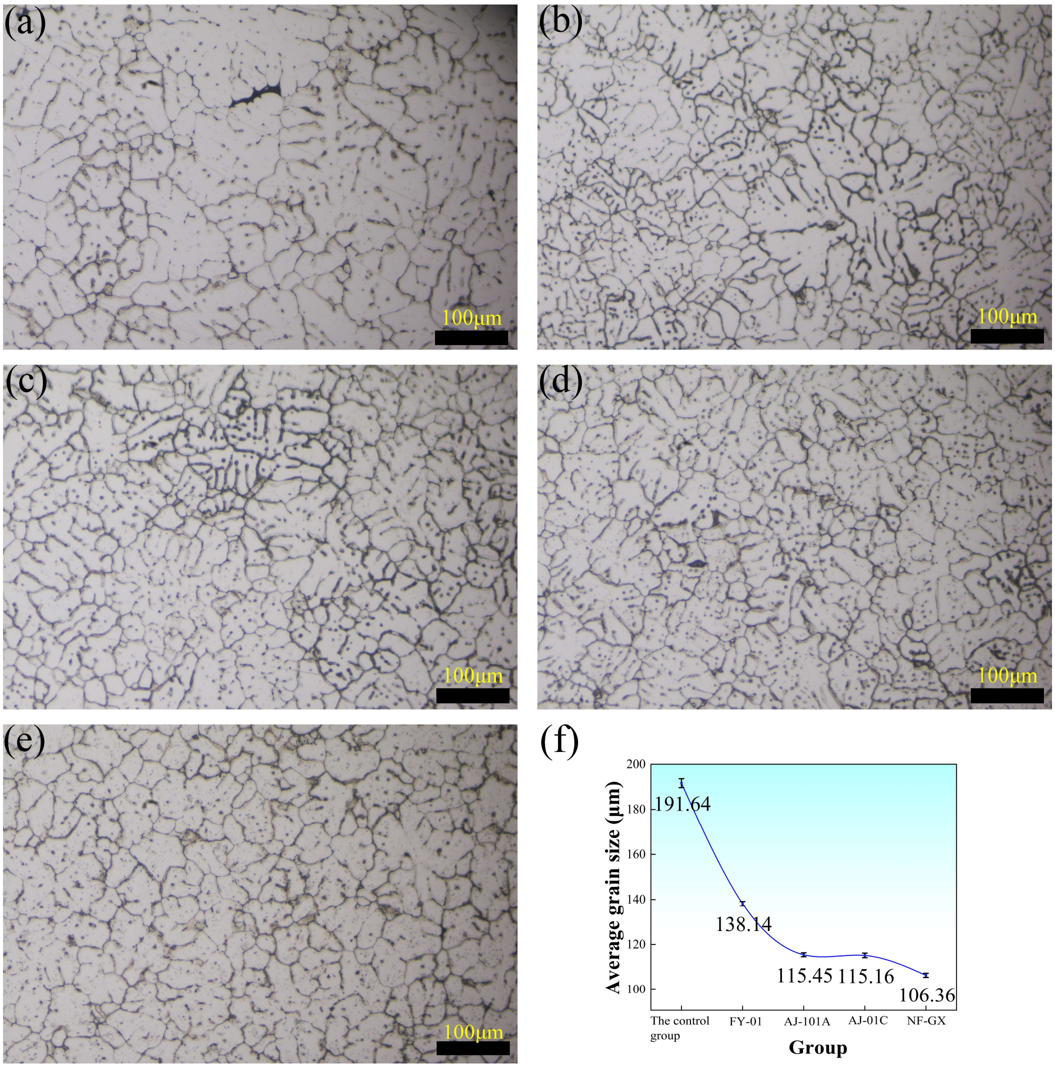

Figure 8. As-cast microstructures of the recycled aluminum alloy treated with different melt purification agents: (a) control group; (b) FY-01; (c) AJ-101A; (d) AJ-01C; (e) NF-GX; and (f) average grain size.

SEM and EDS analyses, shown in Figure 9, provided further insight into microstructural changes. The untreated sample showed significant oxide inclusion aggregation and microporosity at grain boundaries. The EDS point scan results (as shown in Table 7) indicated oxygen contents of 28.18 at.% and 23.75 at.% at points A and C, respectively, confirming the presence of abundant Al_2O_3 inclusions, while point B exhibited high carbon content (22.31 at.%), suggesting residual carbon contamination from the melting process. FY-01 partially removed inclusions but local aggregation remained. AJ-101A further reduced oxide content, likely due to micro-scale agitation from the decomposition of Na_2SiF_6 and Na_2SO_4, promoting inclusion flotation. NF-GX-treated samples displayed clean grain boundaries and a dense microstructure, with no large inclusions. Its multi-component fluoride system could decompose oxide films, dissolve Al_2O_3, and promote inclusion aggregation and flotation, leading to superior melt purification. AJ-01C produced uniform microstructure, but minor residues from $MgCl_2$ and $CaCO_3$ slightly reduced densification.

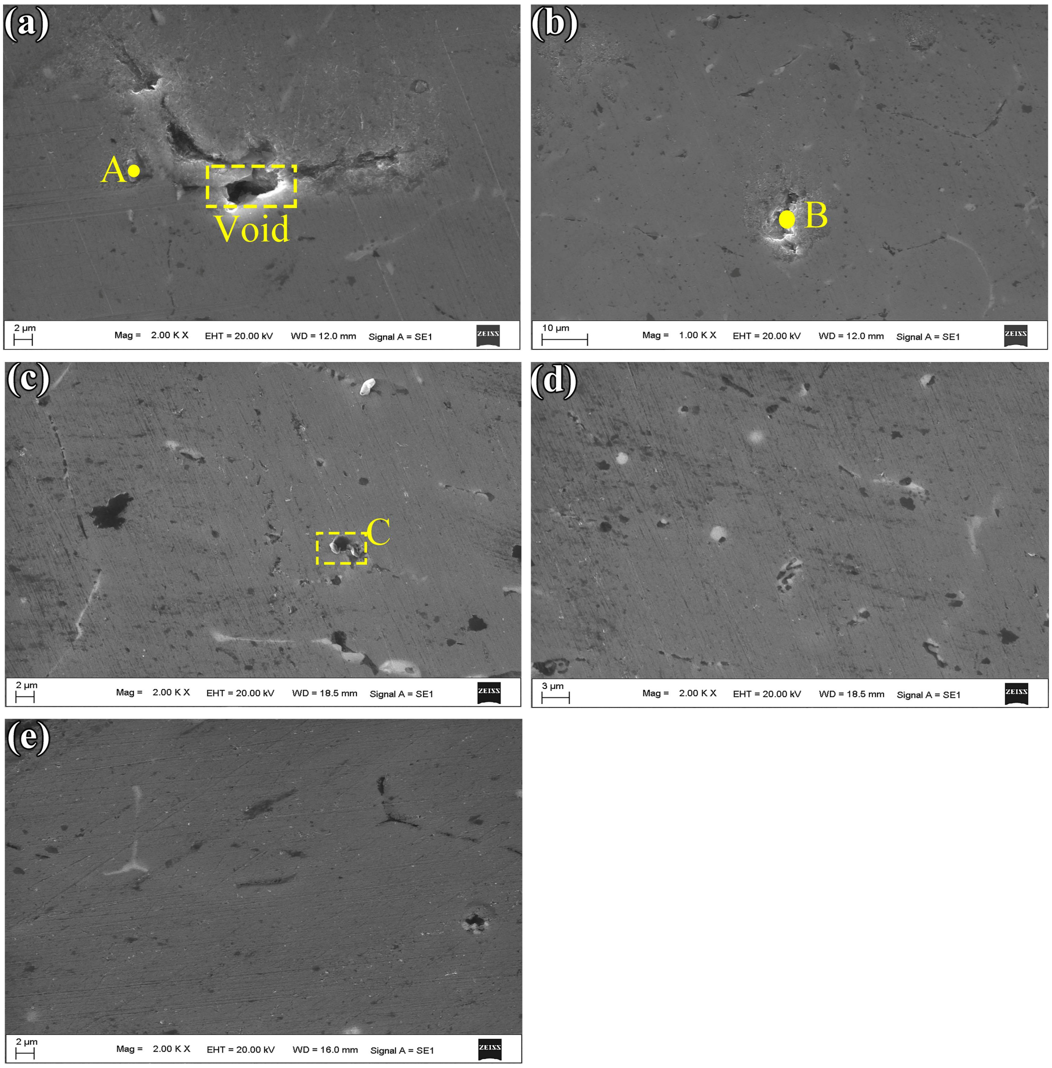

Figure 9. SEM surface morphologies of the recycled aluminum alloy treated with different melt purification agents: (a) control group; (b) FY-01; (c) AJ-101A; (d) AJ-01C; and (e) NF-GX.

Table 7. EDS point analysis results at locations A, B, and C in Figure 9.

Element	Point A (at.%)	Point B (at.%)	Point C (at.%)
Al	67.21	69.92	53.35
O	28.18	5.20	23.75
C	3.38	22.31	15.94
Mg	0.77	1.16	1.22
Cu	0.07	0.41	0.27
Fe	0.04	0.05	0.14

Fracture surface analysis, shown in Figure 10, indicated that the untreated sample exhibited typical brittle features with prominent cleavage planes and few dimples. EDS (as shown in Table 8) revealed the presence of MgO, Fe-rich oxides, and carbon-based contaminants. FY-01 increased dimple density, but cleavage remained. AJ-101A showed more uniform dimples, reflecting better purification. NF-GX produced fully ductile fracture surfaces with evenly distributed dimples and no large inclusions, demonstrating its efficient oxide removal. AJ-01C exhibited intermediate fracture characteristics.

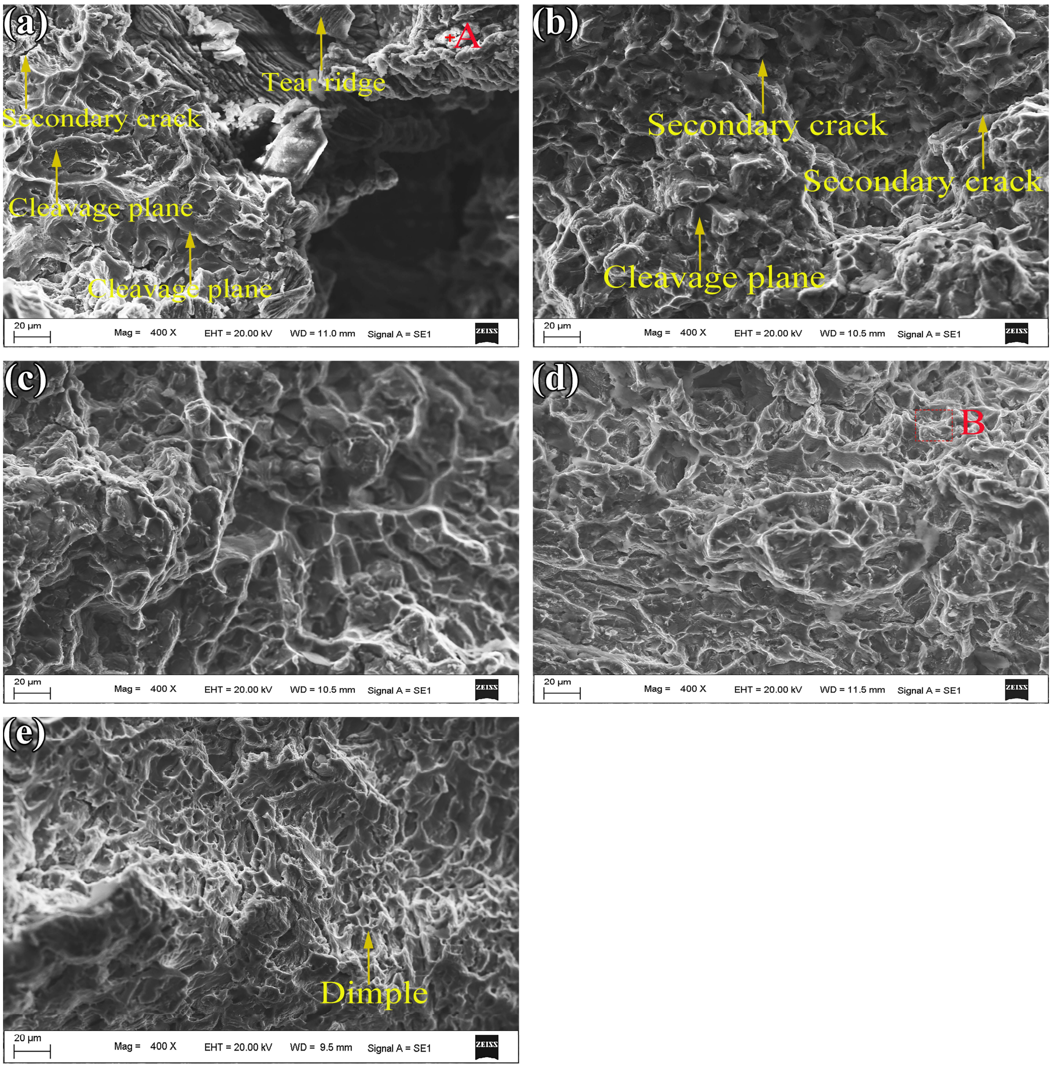

Figure 10. Tensile fracture morphologies of the recycled aluminum alloy treated with different melt purification agents: (a) control group; (b) FY-01; (c) AJ-101A; (d) AJ-01C; and (e) NF-GX.

Table 8. EDS point analysis results at locations A and B in Figure 10.

Element	Point A (at.%)	Point B (at.%)
Al	37.76	25.04
O	36.05	13.89
C	19.29	59.74
Mg	5.38	0.47
Fe	0.67	-
Si	0.84	0.30
Na	-	0.36
Ca	-	0.20

In conclusion, all melt purification agents effectively improved the as-cast microstructure and fracture ductility of recycled aluminum by purifying the melt and providing heterogeneous nucleation sites. The newly designed melt purification agent NF-GX, developed via machine learning, exhibited the most pronounced grain refinement and inclusion removal due to its multi-component system.

5. Conclusions

In this study, we propose a data-driven design strategy for melt purification agents that integrates machine learning, experimental validation, and microstructural characterization, and verify its effectiveness in improving the hot-cracking resistance and mechanical properties of recycled aluminum alloys. This work provides an innovative paradigm for formula development toward high-quality and high-performance recycling of recycled aluminum, effectively breaking through the industrial bottlenecks of traditional empirical trial-and-error methods, such as long development cycles, high experimental costs, and heavy reliance on empirical experience. It also facilitates the large-scale replacement of primary aluminum by recycled aluminum in automotive, high-performance equipment and other engineering fields. Moreover, the established machine learning framework for multi-objective optimization and composition–property correlation analysis exhibits excellent generalization and transferability, which can be readily extended to the customized design of melt purification agents for other non-ferrous alloy systems, including magnesium and copper alloys, as well as for recycled alloys with different impurity characteristics. The major conclusions are summarized as follows:

1. Five machine learning models were evaluated using MAE, RMSE, R^2, and a comprehensive scoring index. RFR showed superior predictive performance for hot-cracking susceptibility and tensile strength. It was consequently adopted as the core model for designing the new melt purification agent.

2. All melt purification agents significantly improved the comprehensive properties of the recycled aluminum alloy, among which the self-developed NF-GX exhibited the optimal modification effect. The model predicted hot-cracking susceptibility and tensile strength of NF-GX of 189.97 and 207.80 MPa, respectively, and the corresponding experimental values were 214.00 ± 10.39 and 191.33 ± 6.11 MPa, respectively, with relative errors of 11.23% and 8.61%, respectively, confirming reliable prediction accuracy of the machine learning model. After treatment with NF-GX, the oxidation loss decreased from 29.19 ± 1.36% to 21.30 ± 0.56%, the hot-cracking susceptibility coefficient reduced from 325.33 ± 11.55 to 214.00 ± 10.39, the tensile strength increased from 152 ± 3 to 191.33 ± 6.11 MPa, and the average grain size was refined from 191.64 ± 1.98

to 106.36 ± 0.92 μm. Microstructural analysis indicated that NF-GX can effectively refine grains, remove oxide inclusions, and improve microstructure compactness, thereby simultaneously reducing oxidation loss and hot-cracking susceptibility and enhancing the mechanical properties of recycled aluminum alloy.

3. Correlation analysis revealed synergistic and competitive interactions among components. The machine learning–designed NF-GX operated through a coupled mechanism of deep melt purification and enhanced heterogeneous nucleation, providing a mechanistic basis for data-driven formulation design and microstructure–property optimization in recycled aluminum alloys.

Use of AI tools declaration

The authors declare they have not used Artificial Intelligence (AI) tools in the creation of this article.

Acknowledgments

This work was supported by the Guangxi Science and Technology Major Project (No. AA24206035), the Guangxi Science and Technology Major Project (No. AA23062026) and the Guangzhou Science and Technology Program (No. 2023A03J0092).

Author contributions

Chengbo Li: conceptualization, methodology, data curation, writing–original draft. Gangzhi Yu: investigation, experimental operation, formal analysis. Honglin Zhou: visualization, data analysis, software. Yan Yan: resources, experimental verification. Zhaowei Wang: validation, data sorting. Tonghan Yang: investigation, sample preparation. Chengyi Huang: software, model simulation. Yuliao Meng: formal analysis, visualization. Xiaoyang Lu: literature collection, data collation. Kaijie Jiang: experiment testing, parameter analysis. Shuanglan Xie: preliminary investigation, technical support. Cailiu Yin: supervision, project administration, funding acquisition, writing–review and editing. All authors have read and agreed to the published version of the manuscript.

Conflict of interest

The authors declare no conflict of interest.

References

1. Yang Y, Zhang H, Wu L, et al. (2024) Supply potential, carbon emission reduction, energy conservation, and sustainable pathways for aluminum recycling in China. *Sustain Prod Consump* 50: 239–252. https://doi.org/10.1016/j.spc.2024.07.034
2. Raabe D, Ponge D, Uggowitzer PJ, et al. (2022) Making sustainable aluminum by recycling scrap: The science of “dirty” alloys. *Prog Mater Sci* 128: 100947. https://doi.org/10.1016/j.pmatsci.2022.100947

3. Gaustad G, Olivetti E, Kirchain R (2012) Improving aluminum recycling: A survey of sorting and impurity removal technologies. *Resour Conserv Recycl* 58: 79–87. https://doi.org/10.1016/j.resconrec.2011.10.010
4. Cai B, Kao A, Lee P, et al. (2019) Growth of β intermetallic in an Al-Cu-Si alloy during directional solidification via machine learned 4D quantification. *Scr Mater* 165: 29–33. https://doi.org/10.1016/j.scriptamat.2019.02.007
5. Du S, Zhang S, Wang J, et al. (2024) Energy flow of aerospace aluminum scraps cycle and advanced integration principles for upcycling technologies: A review. *J Clean Prod* 448: 141176. https://doi.org/10.1016/j.jclepro.2024.141176
6. Su Z, Jin C, Zeng Z, et al. (2024) Simultaneous improvement of mechanical and castability properties of Al-Cu-Mn based alloys by Ca/Ni micro-alloying. *J Alloys Compd* 996: 174824. https://doi.org/10.1016/j.jallcom.2024.174824
7. Li W, Qian F, Li J, et al. (2023) Design strategy for eliminating cracking and improving mechanical properties of Al-Mg-Si alloys fabricated by laser melting deposition. *Addit Manuf* 68: 103513. https://doi.org/10.1016/j.addma.2023.103513
8. Xu Y, Zhang Z, Gao Z, et al. (2021) Effect of Sc on the hot cracking properties of 7xxx aluminum alloy and the microstructure of squeeze castings. *Materials* 14: 6881. https://doi.org/10.3390/ma14226881
9. Yang B, Friedrich S, Friedrich B (2025) Advances in non-metallic inclusion removal from aluminum melts towards cleaner and higher-performance materials. *J Mater Sci* 60: 12291–12314. https://doi.org/10.1007/s10853-025-11195-9
10. Yang B, Gao M, Liu Y, et al. (2023) Formation mechanism of refined Al6 (Mn, Fe) phase particles during continuous rheo-extrusion and its contribution to tensile properties in Al–Mg–Mn–Fe alloys. *Mater Sci Eng A* 872: 144952. https://doi.org/10.1016/j.msea.2023.144952
11. Chen X, Saada MB, Lavisse B, et al. (2025) Recent advances in the remelting process for recycling aluminium alloy chips: A critical review. *Int J Mater Form* 18: 42. https://doi.org/10.1007/s12289-025-01904-9
12. Mair P, Kaserer L, Braun J, et al. (2022) Dependence of mechanical properties and microstructure on solidification onset temperature for Al2024–CaB6 alloys processed using laser powder bed fusion. *Mater Sci Eng A* 833: 142552. https://doi.org/10.1016/j.msea.2021.142552
13. Kim MJ, Yun JP, Yang JBR, et al. (2020) Prediction of the temperature of liquid aluminum and the dissolved hydrogen content in liquid aluminum with a machine learning approach. *Metals* 10: 330. https://doi.org/10.3390/met10030330
14. Datta A, Rana AK, Ghadai RK (2025) Machine learning-driven nonlinear analysis of inclusion effects in aluminium alloys. *Sci Rep* 15: 35866. https://doi.org/10.1038/s41598-025-19756-3
15. Zhang G, Lu W, Wu X, et al. (2023) A new strategy on designing fluxes for aluminum alloy melt refinement. *Materials* 16: 2322. https://doi.org/10.3390/ma16062322
16. Chen X, Zhong J, Lin H, et al. (2024) High precision modeling with stacked neural network to predict the mechanical property of aluminum alloy. *Mater Lett* 375: 137187. https://doi.org/10.1016/j.matlet.2024.137187
17. Cao X, Zhang Y, Li J, et al. (2020) Composition design of 7XXX aluminum alloys optimizing stress corrosion cracking resistance using machine learning. *Mater Res Express* 7: 046506. https://doi.org/10.1088/2053-1591/ab8492

18. Tang J, Aizezi N, Liu J, et al. (2025) A new method for alloy classification based on multimodal fusion of LIBS & exp-LIPA and machine learning. *Opt Laser Technol* 192: 114043. https://doi.org/10.1016/j.optlastec.2025.114043
19. Wang Z, Aizezi N, Ye Y, et al. (2025) Enhanced classification of aluminum alloys via time-frequency dual-domain acoustic feature fusion with laser-induced breakdown spectroscopy. *Talanta* 300: 129208. https://doi.org/10.1016/j.talanta.2025.129208
20. Jiang L, Fu H, Zhang Z, et al. (2024) Synchronously enhancing the strength, toughness, and stress corrosion resistance of high-end aluminum alloys via interpretable machine learning. *Acta Mater* 270: 119873. https//doi.org/10.1016/j.actamat.2024.119873
21. Kwak S, Kim J, Ding H, et al. (2024) Prediction improvement of compressive strength and strain of directionally solidified TiAl alloy based on training data size adjustment. *J Mater Res Technol* 30: 5017–5027. https://doi.org/10.1016/j.jmrt.2024.04.165
22. Fatriansyah JF, Satrio MRR, Federico A, et al. (2024) Machine learning-based forward and inverse designs for prediction and optimization of fracture toughness of aluminum alloy. *Results Eng* 23: 102717. https://doi.org/10.1016/j.rineng.2024.102717
23. Juan Y, Niu G, Yang Y, et al. (2024) Accelerated design of Al-Zn-Mg-Cu alloys via machine learning. *Trans Nonferrous Met Soc China* 34: 709–723. https://doi.org/10.1016/s1003-6326(23)66429-5
24. Abioye SO, Babatunde YO, Abikoye OA, et al. (2025) Optimized machine learning algorithms with SHAP analysis for predicting compressive strength in high-performance concrete. *AI Civ Eng* 4: 16. https://doi.org/10.1007/s43503-025-00061-x
25. Xiong X, Zhang N, Yang J, et al. (2024) Machine learning-assisted prediction of corrosion behavior of 7XXX aluminum alloys. *Metals* 14: 401. https://doi.org/10.3390/met14040401
26. Fu K, Zhu D, Zhang Y, et al. (2023) Predictive modeling of tensile strength in aluminum alloys via machine learning. *Materials* 16: 7236. https://doi.org/10.3390/ma16227236
27. Kim BJ, Kim SH, Kayani SH, et al. (2023) Melt thermal-rate treatment for uniform solute distribution and improved mechanical properties of an Al-Zn-Mg-Cu alloy prepared by direct-chill casting. *J Alloys Compd* 967: 171745. https://doi.org/ 10.1016/j.jallcom.2023.171745
28. Duan Y, Xu G, Peng X, et al. (2015) Effect of Sc and Zr additions on grain stability and superplasticity of the simple thermal–mechanical processed Al-Zn-Mg alloy sheet. *Mater Sci Eng A* 648: 80–91. https://doi.org/10.1016/j.msea.2015.09.049
29. Drezet JM, Mireux B, Kurtuldu G, et al. (2015) Measurement of mechanical coherency temperature and solid volume fraction in Al-Zn alloys using in situ X-ray diffraction during casting. *Metall Mater Trans A* 46: 4183–4190. https://doi.org/10.1007/s11661-015-3041-y
30. Christy JV, Arunachalam R, Mourad A-HI, et al. (2020) Processing, properties, and microstructure of recycled aluminum alloy composites produced through an optimized stir and squeeze casting processes. *J Manuf Process* 59: 287–301. https://doi.org/10.1016/j.jmapro.2020.09.067